Remote Sensing of Environment 191 (2017) 95–109

Contents lists available at ScienceDirect

Remote Sensing of Environment

journal homepage: www.elsevier.com/locate/rse

Using high spatial resolution satellite imagery to map forest burn severity across spatial scales in a Pine Barrens ecosystem

Ran Meng [a,*], Jin Wu [a], Kathy L. Schwager [b], Feng Zhao [c], Philip E. Dennison [d], Bruce D. Cook [e], Kristen Brewster [a,f], Timothy M. Green [b], Shawn P. Serbin [a]

[a] Environmental and Climate Sciences Department, Brookhaven National Laboratory, Bldg. 490A, Upton, NY 11973, USA
[b] Environmental Protection Division, Brookhaven National Laboratory, Bldg. 860, Upton, NY 11973, USA
[c] Department of Geographical Sciences, University of Maryland, 1165 Lefrak Hall, College Park, MD 20742, USA
[d] Department of Geography, University of Utah, 332 S 1400 E, Rm. 217, Salt Lake City, UT 84112, USA
[e] Code 618, Biospheric Sciences Branch, NASA/Goddard Space Flight Center, Greenbelt, MD 20742, USA
[f] Department of Environmental Science and Biology, State University of New York College at Brockport, Brockport, NY 14420, USA

ARTICLE INFO

Article history:
Received 20 June 2016
Received in revised form 9 January 2017
Accepted 15 January 2017
Available online xxxx

Keywords:
Spectral library
Random Forests
Error matrix
Scale effect
Frequency distributions
High spatial resolution

ABSTRACT

As a primary disturbance agent, fire significantly influences local processes and services of forest ecosystems. Although a variety of remote sensing based approaches have been developed and applied to Landsat mission imagery to infer burn severity at 30 m spatial resolution, forest burn severity have still been seldom assessed at fine spatial scales (≤5 m) from very-high-resolution (VHR) data. We assessed a 432 ha forest fire that occurred in April 2012 on Long Island, New York, within the Pine Barrens region, a unique but imperiled fire-dependent ecosystem in the northeastern United States. The mapping of forest burn severity was explored here at fine spatial scales, for the first time using remotely sensed spectral indices and a set of Multiple Endmember Spectral Mixture Analysis (MESMA) fraction images from bi-temporal — pre- and post-fire event — WorldView-2 (WV-2) imagery at 2 m spatial resolution. We first evaluated our approach using 1 m by 1 m validation points at the sub-crown scale per severity class (i.e. unburned, low, moderate, and high severity) from the post-fire 0.10 m color aerial ortho-photos; then, we validated the burn severity mapping of geo-referenced dominant tree crowns (crown scale) and 15 m by 15 m fixed-area plots (inter-crown scale) with the post-fire 0.10 m aerial ortho-photos and measured crown information of twenty forest inventory plots. Our approach can accurately assess forest burn severity at the sub-crown (overall accuracy is 84% with a Kappa value of 0.77), crown (overall accuracy is 82% with a Kappa value of 0.76), and inter-crown scales (89% of the variation in estimated burn severity ratings (i.e. Geo-Composite Burn Index (CBI)). This work highlights that forest burn severity mapping from VHR data can capture heterogeneous fire patterns at fine spatial scales over the large spatial extents. This is important since most ecological processes associated with fire effects vary at the <30 m scale and VHR approaches could significantly advance our ability to characterize fire effects on forest ecosystems.

1. Introduction

Fire is a primary disturbance agent, driving changes in vegetation carbon stocks and shaping ecosystems, as well as influencing the temporal variability in carbon, water and energy fluxes (Bowman et al., 2009; Flannigan et al., 2000; Smith et al., 2016; Sugihara et al., 2006; Werf et al., 2010). In Atlantic coastal Pine Barrens ecosystems, a unique but imperiled ecosystem in the northeastern United States, fire-related management practices including prescribed fire and ecologically sensitive wildfire management must play a key role in restoration and preservation of the hydrological and ecological integrity of these ecosystems (Kurczewski and Boyle, 2000; Jordan et al., 2003). Discrimination of the severity of fire is thus one of the central questions in ecology for examining fire effects on key ecological processes (e.g. tree mortality, post-fire recovery, and intra-species/inter-species competition), and is especially important for fire-related forest management (Frolking et al., 2009; Lentile et al., 2006; Quintano et al., 2013; Sugihara et al., 2006). In wildfire research, the word 'severity' is used to refer the magnitude of change (e.g. extent of vegetation removal, soil exposure, and soil color alteration), caused by fire (Lentile et al., 2006). The Composite Burn Index (CBI) and its modified version GeoCBI have been widely used as means for ground measurements of fire severity (De Santis and Chuvieco, 2009a; Key and Benson, 2006). As an operational tool, (Geo)CBI visually assesses the magnitude of change by fire in

* Corresponding author.
E-mail address: ranmeng@bnl.gov (R. Meng).

http://dx.doi.org/10.1016/j.rse.2017.01.016
0034-4257/

five strata (soils, understory vegetation, mid-canopy, overstory, and dominant overstory vegetation) and integrates these for an overall plot level burn severity rating between zero (unburned) and three (highest severity) (De Santis and Chuvieco, 2009a; Key and Benson, 2006). Although often used interchangeably (Keeley, 2009), a distinction exists between the term burn severity and fire severity, as suggested by Lentile et al. (2006): fire severity refers to short-term (e.g. about within one year following the fire) effects on the local environment, and burn severity refers to both short-term and long-term (up to ten years) effects, including ecological responses (e.g. vegetation recovery). In this study we focus on burn severity given the temporal period of study and scales of interest. Following Lentile et al. (2006) we define three levels of burn severity and use these throughout: consistent with traditional field interpretation of severity in forest ecosystems (Lentile et al., 2006; Veraverbeke et al., 2012) burned sites with >50% green crowns were classified as low severity, those with >50% brown and defoliated (bald) crowns as moderate severity, and those with >50% black (charred) or burned crowns as high severity (Fig. 1)

Compared with time and labor intensive field sampling, remote sensing provides a convenient and consistent way for mapping burned areas or assessing burn severity across large areas (Brewer et al., 2005; Lentile et al., 2006; White et al., 1996). Over the past three decades, a variety of remote sensing-based approaches have been developed and widely applied to Landsat mission imagery to infer burn severity at 30 m spatial resolution (Frolking et al., 2009; Lentile et al., 2006; Jin and Sader, 2005; White et al., 1996). These remote sensing-based approaches for assessing burn severity include remotely sensed spectral indices (SIs, e.g. Lu et al., 2015; Miller et al., 2009; Norton et al., 2009), radiative transfer models (RTM, e.g. Chuvieco et al., 2006; De Santis et al., 2009b), and linear spectral unmixing analysis (LSMA, e.g. Quintano et al., 2013; Riaño et al., 2002). While these remote sensing-based approaches do have some important limitations (for more details see Lentile et al., 2009 for the limitations of an NBR or other similar spectral indices based methods), the differenced Normalized Burn Ratio (dNBR, Key and Benson, 2006; Miller and Thode, 2007) and other spectral indices (Epting et al., 2005; Miller and Thode, 2007; Van Wagtendonk et al., 2004) have been used to assess burn severity across the United States starting as early as 1984 with the Monitoring Trends in Burn Severity Project (MTBS, http://www.mtbs.gov/; Eidenshink et al., 2007). While some previous work suggests the use of an RTM approach, which provides a more physically-based method to estimate burn severity from imagery (Chuvieco et al., 2006; De Santis et al., 2009b), others suggest LSMA is sufficient to assess burn severity (Lentile et al., 2009; Quintano et al., 2013; Smith et al., 2007). LSMA and similar may also be more easily scalable than RTM approaches. LSMA assumes that the reflectance of each mixed pixel can be linearly decomposed by a set of spectrally distinct components (i.e. endmembers) and thus the abundance of endmembers present in that pixel can be estimated (Drake et al., 1999). Recently an expanded version of the standard LSMA, the Multiple Endmember SMA or MESMA (Roberts et al., 1998) has been explored to map burn severity (Fernandez-Manso et al., 2016; Quintano et al., 2013). Compared to the typical LSMA technique, MESMA accounts for endmember within-class spectral variability and overcomes the limitation of using the same number of endmembers to model all pixels (Fernandez-Manso et al., 2016; Quintano et al., 2013).

These remote sensing-based approaches have proven effective for fire monitoring at larger spatial extents (i.e. ≥30 m), but fire effects on forest ecosystems show strong landscape heterogeneity, particularly for wildfires that are not fully stand-replacing or produce a patchy post-fire landscape. As such, post-fire forest structural characteristics and the fire-induced ecological effects often vary at fine spatial scales (≤5 m), and burn severity maps at 30 m (i.e. MTBS) are still too coarse

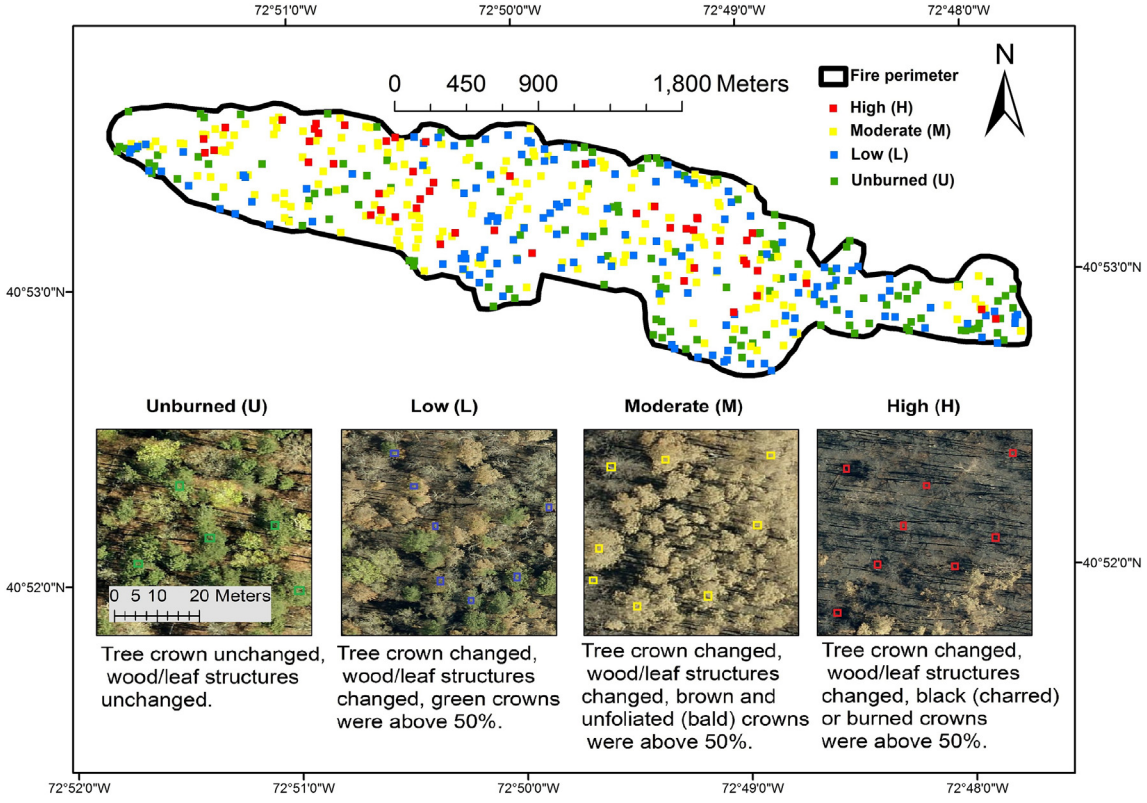

Fig. 1. Definitions of three burn severity levels and unburned classes used in this study. The background photo is the post-fire 0.10 m color aerial ortho-photos in 2012. Spatial distributions of validation points (U (136), L (131), M (190), and H (50) for accuracy assessment of forest burn severity mapping at the sub-crown scale are also shown on the fire perimeter map (see Section 3.5). (For interpretation of the references to color in this figure legend, the reader is referred to the web version of this article.)

to capture the full ecological effects of fire on ecosystems (Holden et al., 2010; Morgan et al., 2014). Increased spatial resolution allows for the improved understanding of plant responses to fire impacts, accurate monitoring of post-fire recovery and ecosystem resilience at a scale relevant to post-fire management or the organisms or system being investigated, while the typical coarse resolution results in inadequate characterization of fire effects in many ecosystem process models (Holden et al., 2010; Morgan et al., 2014; Sparks et al., 2016; Whitman et al., 2013). Therefore, there is a significant need to explore approaches that can map burn severity at fine spatial scales in fire-prone or dependent ecosystems.

The recent increase in the availability of VHR data provides an opportunity to assess forest burn severity at fine spatial scales (e.g. Arnett et al., 2015; Chen et al., 2015a; Dragozi et al., 2016; Holden et al., 2010; Mitri and Gitas, 2006; Mitri and Gitas, 2008). For example, using 1-m post-fire IKONOS imagery, Mitri and Gitas (2008) mapped object-oriented burn severity in open Mediterranean forests. Chen et al. (2015a) also conducted an object-oriented burn severity assessment using a high-spatial (4 m) and high-spectral (50 bands) resolution satellite imagery in diseased forests. While successful, these studies utilized an object-oriented approach, which are highly computationally expensive and often not easily scalable. Other recent studies have highlighted that a pixel-based method can also be used to assess forest burn severity with VHR data (Arnett et al., 2015; Dragozi et al., 2016; Holden et al., 2010). For example, Holden et al. (2010) found that a 3 m QuickBird-derived differenced spectral index from pre-fire to post-fire (i.e. dNDVI, Table 3) showed an improved performance over 30 m Landsat-based dNBR for estimating ground burn severity (R-square = 0.82 and R-square = 0.78 respectively). However, spatial scales between ground measurements of burn severity that cater to ≥30 m pixels and the fine scale satellite measurements (≤5 m) in these past studies show the important mismatch between current approaches and which need revised techniques for VHR imagery. Furthermore, to our knowledge there have not been any previous efforts to explore whether the pixel-based method from VHR data can effectively and consistently map burn severity across different tree species or across spatial scales (i.e. from sub-crown to crown to inter-crown).

We aim to use VHR imagery and a combination of SIs and MESMA to map forest burn severity at fine spatial scales in a Pine Barrens ecosystem (see Methods section). Specifically, we explored: 1) the utility of multiple (>5) SIs for discriminating burned effects at the sub-crown scale. 2) the performance of MESMA fraction images combined with a targeted spectral index from VHR data to map forest burn severity across a fire-prone landscape. We addressed the following questions: 1) does the performance of SIs used in discriminating burned effects vary across different species (i.e. oak and pine) in this ecosystem? And 2) is the burn severity mapping result consistent across spatial scales (i.e. from sub-crown to crown to inter-crown)?

2. Materials

Multiple remotely sensed and ancillary data were used in this study (Table 1). In this section, we first introduce our study area (see Section 2.1) followed by the description of the remotely sensed data and field data collections (see Section 2.2 and Section 2.3).

2.1. Study area

Our study area was located within the Long Island Central Pine Barrens Region within the grounds of the Brookhaven National Laboratory (BNL) and adjacent lands in Suffolk County, New York (Fig. 2). The Nature Conservancy Commission (TNC) has identified Long Island Pine Barrens as a critical habitat with the core area of 21,266 ha protected by Long Island Pine Barrens Protection Act. This region has a moderate-humid climate with evenly-distributed annual precipitation: annual precipitation is approximately 1200 mm; annual daily mean temperature is −4.8 °C in January and 21.9 °C in July (Kurczewski and Boyle, 2000). The sandy-flat soils of this region support pine-oak-heath woodland (Whittaker and Woodwell, 1969). Pitch pine (*Pinus rigida*) is the primary species. Oak species consist of white oak (*Quercus alba* L.) and scarlet oak (*Quercus coccinea*); smaller numbers of black oak (*Quercus velutina* Lam.) are also present. In addition, two main shrub species — huckleberry (*Gaylussacia baccata* K. Koch) and blueberry (*Vaccinium* spp.) — have an inverse canopy cover relationship with tree species (Reiners, 1967).

The 432 ha Crescent Bow fire occurred on April 9, 2012 in the study area (Fig. 2). Post-fire ecological monitoring at point locations within burned areas of BNL has been conducted since the fire. We took digital photos at twenty-three point locations and recorded the photo-view bearings starting two days following the fire (Fig. 2). We revisited the twenty-three point locations and took digital photos at the same photo-view bearings at one-month intervals during the first six months following fire, then in July of each subsequent year. In addition to the photo-view bearing, each photo collected had an associated GPS location and time at which the photo was taken.

2.2. Remotely sensed data

Satellite VHR imagery (Table 2) covering the study area was acquired by WorldView-2 (WV-2) spaceborne platform. WV-2 imagery was available prior to the wildfire on July 17, 2011. Following the wildfire, WV-2 imagery was acquired on September 13, 2012. Only four multi-spectral bands (blue, green, red, and near-infrared2 (NIR2)) were available for the pre-fire WV-2 imagery, due to the data policy of the National Geospatial Intelligence Agency's NextView license agreement. We also acquired NASA Goddard's LiDAR, Hyperspectral and Thermal (G-LiHT; Cook et al., 2013) data on June 15, 2015 but this

Table 1
List of data used in this study.

Name	Spatial resolution	Data acquisition time	Usage
Remotely sensed data			
WorldView-2 (WV-2) imagery	2 m for multi-spectral bands and 0.5 m for panchromatic band	July 17, 2011 and September 13, 2012	Burn severity assessment
NASA Goddard's LiDAR, Hyperspectral and Thermal (G-LiHT) data	1 m	June 15, 2015	Data preprocessing
Post-fire aerial color ortho-photos	0.10 m	May 3, 2012	Reference data for burn severity assessment
Ancillary data			
Plot-based forest inventory measurements	15 m by 15 m	May 2016	Burn severity assessment
MTBS fire perimeter and burn severity map	30 m	Pre-fire Landsat Thematic Mapper (TM) imagery on May 1, 2010; Post-fire Landsat Thematic Mapper Plus (ETM+) imagery on April 28, 2012	Burn severity assessment
Post-fire ecological monitoring photos	N.A.	April 2012 to July 2016	Assistance
USGS DEM	10 m	N.A.	Data preprocessing

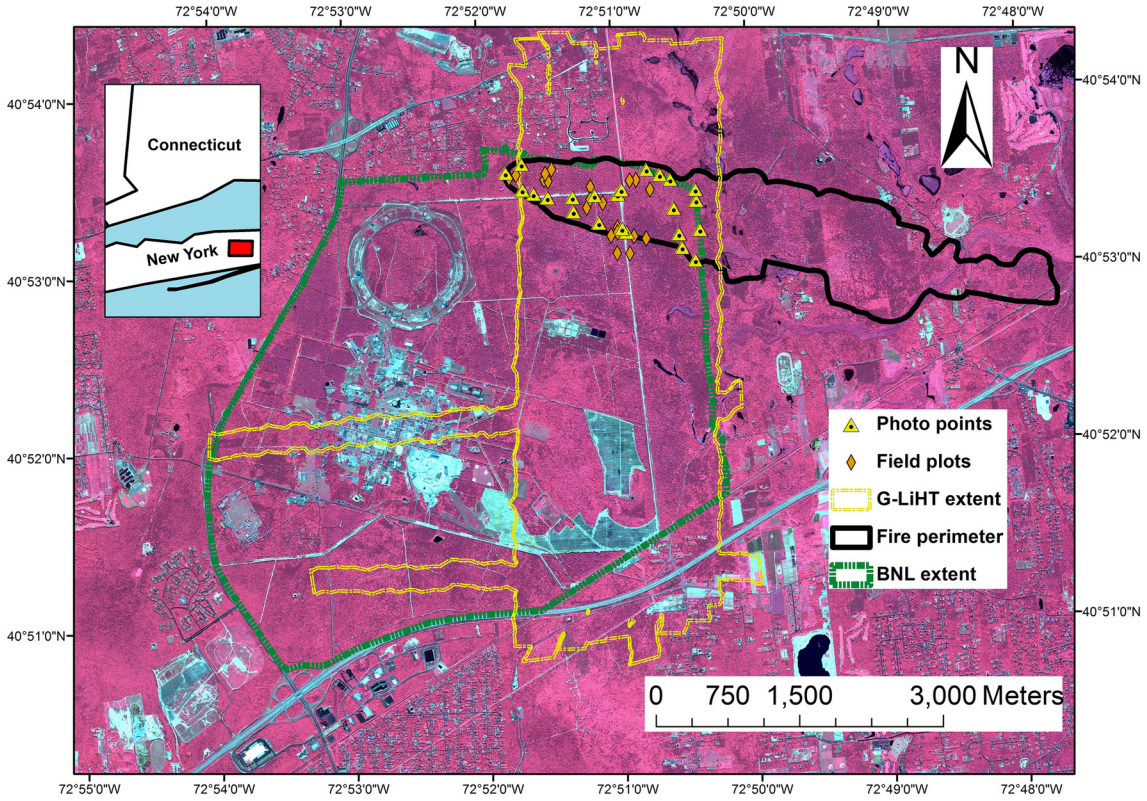

Fig. 2. The study area located within Long Island Central Pine Barrens Region around Brookhaven National Laboratory (BNL) and adjacent areas. The background image is a false color composite of WorldView-2 (WV-2) imagery (near-infrared2 (NIR2)-red-green bands) on July 17, 2011 before the 2012 Crescent Bow fire. (For interpretation of the references to color in this figure legend, the reader is referred to the web version of this article.)

imagery only partially covered the study burned area (Fig. 2). G-LiHT data provides co-registered hyperspectral and LiDAR measurements at high resolutions for environmental studies (Cook et al., 2013). For this study we used the standard G-LiHT at-sensor reflectance product, which was deemed sufficient once we determined atmospheric effects were found to be negligible given the sky conditions and lower altitude of collection during overflight. In addition, we acquired a one-month post-fire 0.10 m ortho-rectified color aerial photography in 2012 covering the burned areas from the New York Statewide Digital Orthoimagery Program (http://gis.ny.gov/).

2.3. Field data collection

In the spring of 2016, we collected forest inventory data derived from 15 m by 15 m fixed-area field plots we established within and around the burn perimeter (Fig. 2, see Section 3.5). A stratified sampling design was used to capture the variations in burned effects across the study area. Our stratification was based on the moderate-resolution MTBS burn severity map and we established and measured five plots within each strata of the MTBS burn severity map (unburned, low, moderate, and high), with a total of twenty plots. Four years post-fire we observed that effects caused by fire (e.g. standing dead trees with burn scars, falling trunks on the ground, open canopy, sparse resprout), were still persistent; unburned areas (e.g. no burn scar on the tree trunks, closed canopies) were also easy to discern in the field. At each plot for all trees with >2.5 cm diameter at breast height (DBH), we recorded the DBH, species, crown condition (vigor, defoliation, burned or dead), crown position (dominant, co-dominant, suppressed, or understory), canopy height, and crown base height (if applicable). Understory species cover and height, as well as canopy cover, were estimated and recorded at 3 m intervals along four transects in the four cardinal directions. Digital photos were taken from the center of each plot to the four cardinal directions to record vegetation structure and soil condition information. Individual tree coordinates and plot centers were recorded with a hand-held decimeter-level differential global positioning system (DGPS, Trimble Geo7x). After differential corrections, the final accuracy of the horizontal position of the sample points was 0.3 m on average.

Table 2
Technical specifications of the WV-2 imagery[a].

Spectral resolution (nm)	*Panchromatic*	450–800
	Coastal	400–450
	Blue	450–510
	Green	510–580
	Yellow	585–625
	Red	630–690
	Red edge	705–745
	Near-infrared1 (NIR1)	770–895
	Near-infrared2 (NIR2)	860–1040
Spatial resolution (m)	Panchromatic	0.5
	Multi-spectral	2

[a] The available bands for the pre-fire imagery in this study is in *italics*.

3. Methods

Our workflow (Fig. 3.) was composed of the following steps: imagery pre-processing (see Section 3.1), the separability analysis of SIs (see Section 3.2), the MESMA procedure (see Section 3.3), burn severity classification (see Section 3.4), and accuracy assessment (see Section 3.5).

After pre-processing WV-2 pre and post-fire images, multiple SIs were calculated. The separability of various SIs in discriminating burned and unburned areas were then compared. Third, as only four bands were available for the pre-fire WV-2 imagery, MESMA was implemented only on the post-fire WV-2 imagery where we had eight bands available. A spectral library was built and image endmembers were included

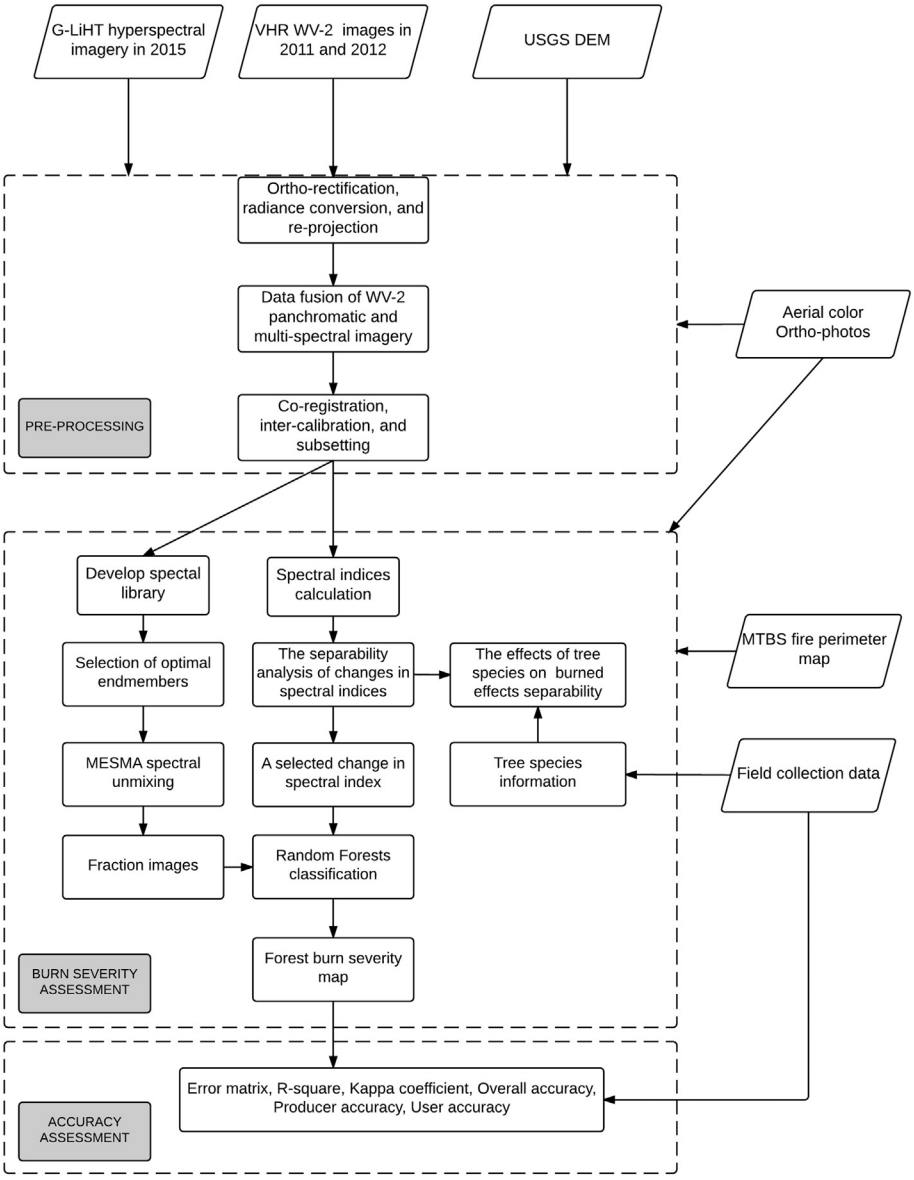

Fig. 3. Flowchart of methodology.

as candidate endmembers (Section 3.4). After selecting optimal endmembers, fraction images were calculated. Fourth, based on the targeted spectral index and fraction images as well as the MTBS fire perimeter, we produced a burned mask and classified burned pixels into three burn severity levels (L, M, and H) using a Random Forests (RF) approach. Finally, the accuracy of the burn severity map was evaluated across spatial scales (sub-crown, crown, and inter-crown)

3.1. Imagery pre-processing

Pre-processing of the remotely sensed data included ortho-rectification, re-projection, radiance conversion, data fusion, co-registration, inter-calibration, and subsetting. All paired panchromatic and multi-spectral band VHR images were retrieved from the DigitalGlobe archive as level 1B (L1B) data through the NASA-NGA Commercial Archive data portal (http://cad4nasa.gsfc.nasa.gov/). L1B imagery had been radiometrically and sensor corrected, but not projected to a plane using a map projection or datum. As a result, all WV-2 images were first ortho-rectified using a 10 m USGS digital elevation model (DEM) with the rational polynomial coefficients (RPCs) supplied for each image and projected to Universal Transverse Mercator coordinate system (UTM, Zone 18 North, World Geodetic System 1984; Fig. 2). To facilitate bi-temporal analysis, WV-2 images in 2011 and 2012 as well as 2015 G-LiHT imagery were co-registered to the post-fire 0.10 m aerial color ortho-photograph in 2012. The co-registration error, i.e., Root Mean Square Error (RMSE), was within 1 m, using 38 ground control points and second order polynomial transformation and nearest neighbor re-sampling. After converting to the at-sensor radiance with the supplied Image MetaData (IMD) file, both of the 2 m multi-spectral WV-2 images were fused with the paired 0.5 m panchromatic WV-2 images to generate pan-sharpened 1 m WV-2 images using Gramm-Schmidt Spectral Sharpening (GSPS) method, consistent with the spatial resolution of the corresponding G-LiHT data. The GSPS method is able to preserve spectral information of the multi-spectral imagery, while enhancing the spatial resolution (Cho et al., 2015; Klonus and Ehlers, 2009).

Previous post-fire multi-temporal analysis has shown that performing a relative normalization correction using Iteratively Re-weighted Multivariate Alteration Detection (IR-MAD) method can produce more consistent temporal reflectance response than absolute atmospheric corrections, when processing time-series imagery with spatial and temporal consistence (Schroeder et al., 2006). As a result, inter-calibration was performed between the G-LiHT at-

sensor reflectance image and the pan-sharpened 2011 and 2012 WV-2 images using IR-MAD method for radiometric normalization, instead of absolute atmospheric corrections (Canty and Nielsen, 2008). As a radiometric normalization method, IR-MAD method fits a linear regression model for each spectral band, on the basis of bi-temporal invariant pixels by iterative canonical correlation (Canty and Nielsen, 2008). Before the inter-calibration, G-LiHT at-sensor reflectance image was used to simulate multispectral WV-2 imagery, according to the sensor response function in ENVI 5.3 (http://www.harrisgeospatial.com/).

3.2. The separability analysis of SIs in discriminating burned effects

To assess the separability of SIs in discriminating burned effects from VHR across different species (i.e. oak and pine), we calcualted SIs from the bi-temporal WV-2 imagery in 2011 and 2012, respectively. Then, we manually extracted unburned and burned pixels of different pre-fire canopy species composition (i.e. pine and oak) directly on the bi-temporal WV-2 imagery from the field inventory data. Finally, the separability analysis of SIs was perfomed.

3.2.1. SIs calculations

Although often lacking the shortwave-infrared band, SIs analysis from VHR data has shown promise for improving assessments of burn severity (Arnett et al., 2015; Dragozi et al., 2016; Holden et al., 2010). SIs are typically used to reduce effects of topography, viewing angle, sun angle, and radiometric consistency for change detections of bi-temporal imagery (Hart and Veblen, 2015). After imagery pre-processing, we calculated a range of SIs (i.e. NDVI, EVI, SAVI, MSAVI, BAI, and RVI, Table 3) that have been used to map fire effects and burned areas (e.g. Chuvieco et al., 2002; Schepers et al., 2014). RGI and BR have been used previously as an indicator of bare ground during the detection of beetle-induced tree mortality (Coops et al., 2006; Hart and Veblen, 2015), and we expected they could be used to identify increased visible bare ground within the burned areas as a result of fire-caused canopy loss.

The changes in SIs from post-fire to pre-fire were calculated to characterize the temporal change in those pixels identified as containing well-lit tree foliage in the 2011 image. For these SIs, the changes were calculated as Eq. (1).

$$\Delta SI = SI_{\text{pos-fire}} - SI_{\text{pre-fire}} \tag{1}$$

where ΔSI is the change in the spectral index from the post-fire image to pre-fire image. The difference in viewing geometry and illumination conditions are some of the challenges in change detection of individual trees through time using bi-temporal VHR imagery (Wulder et al., 2008). In this study, we chose to isolate image pixels containing well-lit vegetation from those containing shade. Specifically, we first masked apparent cloud and cloud shadow areas manually from the WV-2 images in 2011 and 2012. Then, we masked the 2011 WV-2 imagery to retain well-lit vegetation pixels with an NDVI ≥0.70 and at-sensor NIR reflectance ≥10% for subsequent analysis (Marvin et al., 2016).

3.2.2. The separability analysis

A separability index (Eq. (2)) was used to estimate the effectiveness of the eight ΔSI to discriminate burned and unburned class.

$$M = \frac{|\mu_b - \mu_u|}{\sigma_b + \sigma_u} \tag{2}$$

where μ_b and μ_u are the mean values of the considered ΔSI of burned and unburned class, and σ_b and σ_u are the corresponding standard deviations. The separability index has been frequently used to assess the degree of discrimination in fire ecology studies for both broadband and imaging spectroscopy sensors (e.g. Pereira, 1999; Schepers et al., 2014). The higher the separability value, the better the discrimination. A value of $M < 1$ denotes that the histograms overlap between the unburned and burned class and the ability to separate the two pixel groups is poor, while a value of $M > 1$ represents a good separability.

We overlaid the geo-referenced points of unburned and burn-killed trees, derived from field inventory data, directly on the bi-temporal WV-2 imagery, and then we manually extracted unburned and burned pixels of tree crown with high confidence through visual inspections (Fig. 4). During this process, 97 black/brown tree crowns (49 oak and 48 pine) and 73 unburned tree crowns (28 oak and 45 pine) were used. In total, this yielded 495 burned pixels and 505 unburned pixels.

3.3. MESMA procedure

Compared with a basic LSMA analysis, MESMA allows the number and types of endmembers to vary on a per-pixel basis (Roberts et al., 1998). Specifically, MESMA can be used to estimate image fractions, in which variable endmember models (e.g. two, three, four or even larger than four) with different number of endmembers are combined to produce a single fraction map, while minimizing per-pixel basis Root Mean Square Error (RMSE) and maintaining fraction constraints by selecting the best-fit model for each pixel (Roberts et al., 2015). In this study, the MESMA procedure consisted of three key steps. First, we developed a spectral library. Second, we selected the optimal endmembers to form our final spectral library. Third, we ran MESMA to calculate the fraction images based on the image endmembers. All of the MESMA-related procedures in this study were implemented in the Visualization and Image Processing for Environmental Research (VIPER) tools software package (Roberts et al., 2007) integrated within ENVI 5.3.

Table 3
Spectral indices used to classify tree species and assess forest burn severity[a].

Spectral Index	Abbreviation	Formula	References
Normalized Difference Vegetation Index	NDVI	$\frac{NIR2-R}{NIR2+R}$	(Tucker, 1979)
Enhanced Vegetation Index	EVI	$\frac{2.5(NIR2-R)}{NIR2+6R-7.5B+1}$	(Huete et al., 2002)
Soil Adjusted Vegetation Index	SAVI	$\frac{(1+L)(NIR2-R)}{NIR2+R+L}$ with L = 0.5	(Huete, 1988)
Modified Soil Adjusted Vegetation Index	MSAVI	$\frac{2NIR2+1-\sqrt{(2NIR2+1)^2-8(NIR2-R)}}{2}$	(Qi et al., 1994)
Burned Area Index	BAI	$\frac{1}{(0.1+R)^2+0.06+NIR2}$	(Chuvieco et al., 2002)
Red-Green Index	RGI	$\frac{R}{G}$	(Coops et al., 2006)
Blue-Red Index	BR	$\frac{B}{R}$	(Hart and Veblen, 2015)
Ratio Vegetation Index	RVI	$\frac{NIR2}{R}$	(Davranche et al., 2010)

[a] R: WV-2 red band; B: WV-2 blue band; G: WV-2 green band; NIR2: WV-2 near-infrared2 band.

Fig. 4. Ground-truth tree crown points in the field and corresponding onsite digital photos. The background image is the post-fire WV-2 false color image (NIR2-red-green bands) on September 13, 2012. (For interpretation of the references to color in this figure legend, the reader is referred to the web version of this article.)

3.3.1. Spectral library development

Two alternatives exist for developing a spectral library: collection of image endmembers from the image or using reference endmembers from other spectral libraries or sources (Settle and Campbell, 1998). We used image spectra to define endmembers given the simplicity of obtaining "pure" endmembers with VHR imagery with high confidence and because they would have the same scale of measurement as the data. Specifically, following Dudley et al. (2015), based on our knowledge of the study area from our field surveys, we manually defined potential endmembers on the post-fire aerial color ortho-photograph using a set of uniform georeferenced polygons for each class. The post-fire WV-2 imagery and color aerial ortho-photos were acquired within about five months and one month after the fire, respectively. Most short-term fire effects (e.g. ash, scorched canopy, standing trunk) had not diminished in the imagery. During this process, we selected at least one hundred endmembers per class.

3.3.2. Selection of optimal endmembers

Identifying a set of high quality endmembers is a critical stage of MESMA. Following Quintano et al. (2013) and Fernandez-Manso et al. (2016), we used the following three criteria to select the most appropriate endmembers: 1) Count-based Endmember Selection (CoB) - endmembers modeling the greatest number of the candidate endmembers within a class are selected (Roberts et al., 2003); 2) Endmember Average RMSE (EAR) - endmembers producing the lowest EAR within a class are selected (Dennison and Roberts, 2003); 3) Minimum Average Spectral Angle (MASA) - endmembers having the lowest spectral angle within a class are selected (Dennison et al., 2004). We combined these three criteria for final selections. Using EAR, we selected endmembers producing the least EAR within their class. When MASA was considered, we chose endmembers having the lowest spectral angle within a class. When taking CoB into account, endmembers modeling the greatest number of candidate endmembers within their class were chosen. In addition, we considered the typical spectral shape of the candidate endmembers, based on our knowledge of the study area and spectroscopy.

3.3.3. Spectral unmixing modeling

After selecting the optimal endmembers using the above-mentioned measures, we grouped them into three different spectral libraries including green vegetation (GV), non-photosynthetic vegetation (NPV) or ash, and soil or other non-vegetation (NV). Shade was also present in all pixels. We assumed every original post-fire WV-2 pixel can be modeled by a linear combination of these two, three, or four endmembers. In this study we set the MESMA fraction constraints at −5 to 105%; maximum allowable shade fraction at 100%; and maximum allowable RMSE at 0.025. In addition, a threshold of 0.003 change in RMSE (reflectance units) was selected empirically to determine whether a two, three, or four-endmember models should be used for each pixel. In the case of a tied RMSE the model with the lowest RMSE was used.

3.4. Burn severity classification

A multi-step classification method was applied to map forest burn severity, using both a ΔSI and MESMA fractions. First, by dividing each endmember by the total percent of all non-shade endmember in a pixel, shade-normalization was performed on the fraction images to suppress the shade fraction and emphasize the relative abundance of

non-shade endmembers. Secondly, we identified the burned pixels, using the combination of the targeted Δ SI in Section 3.2 and MESMA fraction images produced in Section 3.3: a ΔSI from post-fire to pre-fire indicated canopy loss, the dominant burned effects in a forest ecosystem; MESMA made use of the full spectra to estimate post-fire fractional cover components, directly analogous and scalable to burn severity definition of this study. Following Quintano et al. (2013) and the previous separability analysis of SIs, we selected burned pixels that simultaneously met four conditions: 1) Δ MSAVI was less than a threshold of −0.08 (see Section 4.1); 2) their NPV fraction was higher than the average of the image; 3) their GV fraction, excluding a "grass" and "shrub" endmember, was lower than the average; 4) Pixels were within the MTBS fire perimeter. Third, we applied the "burned mask" to the shade-normalized fraction images.

We used a RF approach in our classification model with five hundred trees to classify three burn severity levels (L, M, and H). RF is a good choice for our analyses as it is not sensitive to predictor multicollinearity and able to find the best predictor variables (Speybroeck, 2012). Importantly, RF is a supervised machine learning technique that is widely used by the remote sensing community (e.g. Lawrence et al., 2006; Meng et al., 2012; Meng and Dennison, 2015; Pal, 2005; Yu et al., 2011). As a non-parametric decision-tree based classifier, RF makes no assumption about the underlying distribution of the data and corrects the habit of overfitting of traditional decision tree methods, leading to high accuracy and robust results (Breiman, 2001). RF has an internal unbiased estimate of the training set error called the out-of-bag (OOB) error (Breiman, 2001). Our RF classifier was constructed from bootstrapped samples comprising about two-thirds of the training dataset; training samples not used in the RF construction were put in the tree classifier to get a classification. The ratio of the times that a class is not the true class across all bootstrap iterations is called the OOB error estimation (Breiman, 2001).

In order to train the trees of the RF, a minimum of eighty pixels per burn severity level (L (125), M (146), and H (80)) was selected and defined from the 0.10 m post-fire aerial color ortho-photos, as ground reference. As a preliminary analysis, we ran RF classifications for different combinations of explanatory variables to compare the predictive power by internal OOB error estimation: Δ MSAVI (28.41%), shade normalized MESMA fractions (21.03%), and Δ MSAVI plus MESMA fractions (15.13%). We thus chose to use both the masked shade normalized fraction images and Δ MSAVI for burn severity classification. After the classification process, a 3 by 3 median filter was applied to the RF classified image to remove outliers or impulse-like noises, which is a common post-classification procedure helpful for increasing the accuracy used in previous MESMA-based burn severity mapping studies (Fernandez-Manso et al., 2016; Quintano et al., 2013).

3.5. Accuracy assessment

We assessed the forest burn severity classification in this study at the sub-crown, crown, and inter-crown scales. For the sub-crown scale validation, we first generated a minimum of fifty validation points per class through stratified sampling based on the generated WV-2 burn severity map. Then, considering the three burn severity levels (L (131), M (190), and H (50)) as well as unburned class (136), the generated validation points were defined from the post-fire 0.10 m color aerial ortho-photos as ground reference (Fig. 1). The sample unit of validation points is a rectangle of 1 m by 1 m. Classification of each validation point was determined through visual inspection of the most frequent burn severity class within each rectangle. Finally, the error matrix of RF burn severity classification was generated. Overall accuracy (OA), Kappa value, producer's accuracy (PA) (omission error), and user's accuracy (UA) (mission error) for each class were calculated and reported (Congalton, 1991a; Congalton, 1991b).

For the crown scale validation, we first delineated the crowns of each geo-referenced dominant tree with field measurements and the post-fire 0.10 m color aerial ortho-photos. Similar to the sub-crown scale validation, each dominant tree crown was defined (U (73), L (22), M (37), and H (74)) through visual inspection of the post-fire 0.10 m color aerial ortho-photos as ground reference by the most frequent burn severity class within it. The corresponding OA, PA, UA, and kappa value of RF burn severity classification were also calculated and reported.

For our study we did not have access to GeoCBI plot survey data within one year following the fire; four years post-fire we conducted forest inventory survey to estimate long-term burned effects with twenty 15 m by 15 m fixed-area field plots. However, a strong correlation (R-squared = 0.85) was found between the percentage of black/brown crowns (an indicator for burn severity) and GeoCBI ratings on eighty-nine 30 m by 30 m sample plots using Eq. (3) (Veraverbeke et al., 2012).

$$\mathrm{GeoCBI} = 1.81 \times X + 0.89 \tag{3}$$

where X is the black/brown tree percentage within a field plot. We directly applied the Eq. (3) for predicting GeoCBI in this study, as the same vegetation type (i.e. mixed evergreen and deciduous forests with well-drained soils) was investigated. Therefore, for the inter-crown scale validation, we first calculated the black/brown tree percentage within each field plot, through the 0.10 m post-fire color aerial ortho-photos (short-term effects) and forest inventory measurements four years following the fire (the long-term effects). We then extracted and calculated the mean values of MESMA image fractions (e.g. GV, NPV-ash, and soil-NV) and ΔMSAVI within each field plot. We also calculated the corresponding twenty plot GeoCBI ratings by the black/brown tree percentage using Eq. (3). Finally, using mean values of MESMA image fractions and ΔMSAVI, as predictor variables, we modeled the GeoCBI ratings of field plots, using an ordinary least squares (OLS) regression approach. The presence of spatial autocorrelation in plot GeoCBI rating was also verified by global Moran's I statistics (0.344, $p < 0.001$). As a result, a spatial filtering technique was incorporated into the OLS model to deal with the spatial effects (Griffith and Peres-Neto, 2006). Importantly, Meng et al. (2015) found the spatial filtering technique used in this analysis had the best performance among several spatial modeling techniques (e.g. spatial autoregressive, spatial filtering, geographically weighted regression), in terms of efficiency and accuracy. A threshold value of 10 on the variance inflation factor (VIF) was used to determine the multi-collinearity of predictor variables (Craney and Surles, 2002). Predictor variables showing multi-collinearity were dropped from the OLS model one by one, with the order of R-squared contributions, until all multi-collinearity was removed. The larger variations in plot GeoCBI ratings explained by the final OLS model, the higher accuracy in predicting the inter-crown scale ground measurements of burn severity from remotely sensed measurements of VHR data. The OLS regression approach and the spatial filtering technique were both conducted in R environment (Team, 2013).

In addition, three burn severity levels (L, M, and H) of field plots were defined, according to the estimated GeoCBI ratings (De Santis & Chuvieco, 2009a). The unburned class (U) of field plots was defined directly through visual inspections of the post-fire 0.10 m color aerial ortho-photos and field measurements. In each group of the GeoCBI-defined plots (15 m by 15 m fixed-area), the average percentages of pixels (1 m by 1 m) dominated by black canopy, brown (non-foliated) canopy, post-fire green canopy, and unburned canopy were calculated and reported.

4. Results

4.1. The separability of ΔSI in discriminating burned effects from VHR data

The separability index (M) values for each ΔSI are listed in Table 4. ΔMSAVI had the highest M value (M = 2.043). Followed by the Δ

Table 4
M index values comparing unburned and burned separability for ΔSI.

ΔSI	Separability index values (M)
ΔMSAVI	2.043
ΔSAVI	2.018
ΔEVI	1.182
ΔNDVI	0.166
ΔBAI	0.100
ΔRVI	0.079
ΔRGI	0.067
ΔBR	0.015

MSAVI, ΔSAVI and ΔEVI both demonstrated high discriminatory power (M = 2.018 and M = 1.182, respectively). The ΔNDVI (M = 0.166), the ΔBAI (M = 0.166), the ΔRVI (M = 0.100), the ΔRGI (M = 0.079), and, especially, the ΔBR (M = 0.015) had very low M values. According to the ΔSI discrimination results, ΔMSAVI was selected for subsequent forest burn severity mapping.

To better understand if the performance of ΔSI to discriminate burned effects depended on tree species, we also calculated the M values for the targeted ΔSI (ΔMSAVI) by tree species (Table 5). We found that the sensitivity of ΔSIs did not show a dependency on tree species (i.e. pine and oak) when using VHR imagery. As a result, we did not perform forest burn severity analysis on a tree species basis.

The frequency distributions of burned and unburned tree crown pixels extracted in Section 3.2 are shown for ΔMSAVI in Fig. 5. Consistent with ΔSI discrimination results, the histograms of burned and unburned were well separated and relatively easy to discriminate for ΔMSAVI (M = 2.043). The frequency distribution of unburned tree crown pixels was within the upper range, compared with the frequency distribution of burned tree crown.

4.2. MESMA procedure

Our GV endmembers include oak, pine, wetland, shrub, and grass; NPV-ash endmembers include ash and non-photosynthetic plants; and soil-NV endmember NIR include impervious surface, soils, waterbody, and cloud (Table 6). Fig. 6 provides some example endmember spectra derived from the post-fire WV-2 image. For example, Fig. 6a shows that, in general, the oak canopies had the highest reflectance in the NIR followed by grass and shrub canopies, while pine and wetland areas had the lowest NIR reflectance. We also found a large range in char/ash reflectance that had a lower albedo than NPV (Fig. 6b); as expected water had the lowest albedo.

Fig. 7 provides our shade-normalized fraction images from the post-fire WV-2 imagery in 2012. In these images the brighter the pixels the higher the fraction. GV and NPV-ash fraction images clearly show the burned effects. Soil-NV fraction images also clearly identify bare soils, small trails, buildup areas, waterbody, cloud, and small roads. Pixels contaminated by cloud show highest modeling errors on the RMSE fraction imagery. In total, 96.2% of the image pixels were unmixed by MESMA with 249 models.

Table 5
M index values comparing burned effects separability by tree species for ΔMSAVI.

ΔSI	Burned effects-tree species vs. burned effects-tree species	Separability index values (M)
ΔMSAVI	Burned pine vs. unburned pine	1.605
ΔMSAVI	Burned oak vs. unburned oak	1.827
ΔMSAVI	Unburned oak vs. unburned pine	0.032
ΔMSAVI	Burned oak vs. burned pine	0.045

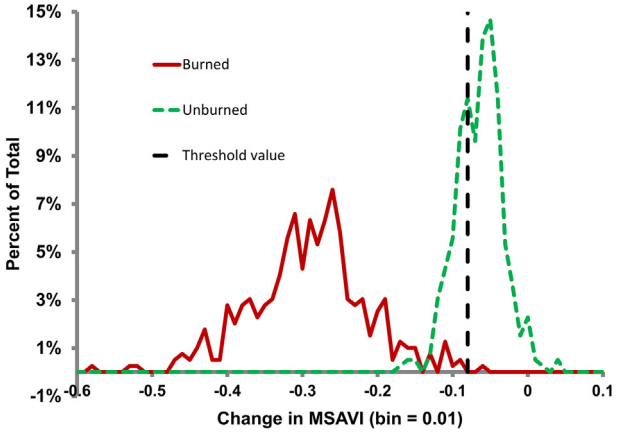

Fig. 5. Frequency distributions of burned and unburned extracted tree crown pixels for ΔMSAVI. The vertical dash lines show a threshold value of −0.08 for discriminating burned pixels in Section 3.4.

4.3. Burn severity classification

Based on the previously mentioned ΔMSAVI and MESMA fraction images, the forest burn severity map was classified by a multi-step classification method (Fig. 8). The heterogeneity of the burned area is clearly apparent but, importantly, the overall pattern matches that of the MTBS map (Fig. 8): some small unburned or low-severity patches were found to be bordered by large moderate- to high-severity patches; especially for the high severity and unburned class, their spatial distributions were more widespread on the WV-2-based map. We found that the spatial resolution of the Landsat-based MTBS (i.e. 30 m pixel size) reduced the number of burn severity levels it could resolve as compared to the WV-2 imagery. As a result, our WV-2-based ΔMSAVI and MESMA map displayed more spatial detailed burned effects, fire patterns, and heterogeneity with specific ecological means (i.e. green canopies, brown or bald canopies, charred canopies), compared with the Landsat-based dNBR MTBS map (Fig. 8).

4.4. Accuracy assessment

OA, PA, UA, and Kappa (see Section 3.5) at the sub-crown and crown scales were calculated, respectively (Table 7). The burn severity map shows high OA (84%) and Kappa value (0.77) at the sub-crown scale. Unburned and high-severity classes had high values in UA (>80%) and PA (>80%), low-severity class had acceptable moderate values in UA (>70% and <80%) and PA (>70% and <80%), while moderate-severity had unbalanced high values in UA (>80%) and moderate values in PA (>70% and <80%). The crown scale accuracy assessment had similar overall performances to the sub-crown

Table 6
MESMA spectral libraries.

Spectral library	Endmember name	Number of Endmembers	Number of Samples
GV	Oak	2	680
	Pine	2	590
	Shrub	2	452
	Grass	2	328
	Wetland	1	189
NPV-ash	Ash	2	190
	NPV	2	189
Soil-NV	Impervious surface	2	630
	Soil	2	236
	Waterbody	1	208
	Cloud	1	156

Note: GV: green vegetation; NPV: non-photosynthetic vegetation; NV: non-vegetation.

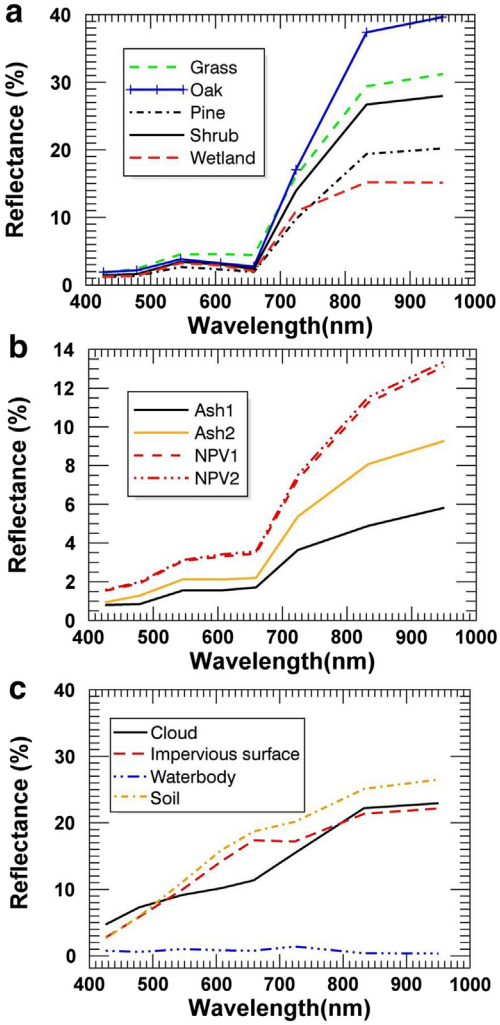

Fig. 6. Example WV-2 spectra from the spectral libraries for MESMA. a. GV spectral library; b. NPV-ash spectral library; c. soil-NV spectral library.

scale accuracy (OA = 82%; Kappa value = 0.76). Unburned and high-severity classes had high values in UA (>80%) and PA (>80%); low-severity class had an acceptable value in PA (75%), but a low value in UA (50%), caused mainly by the confusion with moderate-severity class; moderate-severity class had acceptable balanced values in UA (70%) and PA (75%).

The final OLS model for predicting the plot GeoCBI ratings is shown as Eq. (4). Mean soil-NV fraction and ΔMSAVI can explain 89% variations in estimated GeoCBI from twenty 15 m by 15 m fixed-area field plots. All the predictor variables were significant at 0.05 confidence level.

$$Y = -33.179 \times \text{Soil-NV} - 9.555 \times \Delta\text{MSAVI} + 1.013 \quad (4)$$

where Soil-NV is the mean soil-NV fraction, and ΔMSAVI is the mean change in MSAVI, calculated from all the valid WV-2 pixels within a 15 m by 15 m fixed-area field plot. GV and NPV-ash fractions were dropped from the final OLS model, because they both had multi-collinearity and less R-squared contributions, compared with ΔMSAVI. Fig. 9 shows the scatterplot of estimated plot GeoCBI and corresponding OLS model predicted values. The high correlation (Adjusted R-squared = 0.89) shows that remotely sensed measurements at the sub-crown scale can be used to predicting the inter-crown scale ground measurements of burn severity (e.g. GeoCBI) with high confidence.

The mean percentages of classified pixels (black canopy, brown canopy, post-fire green, and unburned canopy) within GeoCBI–defined plots are summarized and shown in Fig. 10. Canopy class percentages were significantly different among severity groups from GeoCBI-defined field plots, but indicated a general agreement between satellite burn severity classification and field plot based results at the inter-crown scale: the mean percentages of unburned canopy decreased with severity level, but black and especially brown canopies indicated an opposite trend. Importantly, it is clear that burn severity mapping at fine spatial scales from VHR satellite measurements was consistent with the standard inter-crown scale measurements (GeoCBI). Moreover, consistent with Fig. 8, Fig. 10 indicates the heterogeneity of burn severity patterns was high at the inter-crown scale. Specifically, except the unburned group, all four burned effects related canopy classes can be found in other severity groups. The large standard deviation in the high severity group also indicated the uncertainty caused by the GeoCBI-defined burn severity classification.

5. Discussion

Burn severity mapping is critical to the understanding of long term post-fire recovery trends and ecosystem resilience (Fernandez-Manso et al., 2016; Morgan et al., 2014; Smith et al., 2016; Wilson et al., 2015). As a result a number of studies using coarse- to moderate-resolution satellite observations (e.g. 30 m Landsat series) have been widely conducted (De Santis and Chuvieco, 2009a; Key and Benson, 2006; Lentile et al., 2006). Since fire effects can vary at different scales, one spatial or temporal scale may not be appropriate to address all objectives for assessing burn severity (Morgan et al., 2014). The increased availability of VHR imagery provides an important opportunity to map burn severity and monitor post-fire succession at fine spatial scales. And these fine scale burned effect studies will be useful for a number of ecological management activities (e.g. Pine Barrens restoration, ecologically sensitive fire suppression in wildland–urban interface, Mitri and Gitas, 2013; Pérez-Cabello et al., 2012) and the development of consistent and transferable quantifications of burn severity (e.g. the changed ability of the plant to assimilate carbon by fire) across spatial scales or fire regimes (Morgan et al., 2014; Smith et al., 2016). In this study we explored forest burn severity mapping for the first time using remotely sensed SIs and a set of MESMA fraction imagery (e.g. GV, NPV-ash, and soil-NV) from VHR data in a Pine Barrens ecosystem.

Our evaluation of the resulting burn-severity map indicated that our approach not only can be used for forest burn severity mapping at fine spatial scales from VHR data with reasonable accuracy (Table 7 and Fig. 9), but also showed that the results were consistent across spatial scales. As such we observed that VHR data can provide valuable information on burned effects from the sub-crown to crown to inter-crown scales. Furthermore, previous studies indicated that SIs could accurately quantify changes in plant physiology caused by fire at the leaf level (Smith et al., 2016; Sparks et al., 2016). Thus burn severity mapping at fine spatial scales using ΔSI and MESMA fractions can provide not only more spatial details for informing fire-related ecological studies and management, but could also provide additional insights on changes in plant function associated with fire impacts (Morgan et al., 2014; Smith et al., 2016).

Importantly in this study we found that our results using VHR data showed much more spatial details than that derived from the Landsat-based MTBS burn severity product at 30 m (Fig. 8). Heterogeneity in specific burned effects in these areas cannot be resolved by 30 m Landsat data (Holden et al., 2010; Arnett et al., 2015; Dragozi et al., 2016). As a result, the 30 m Landsat pixels usually include a mix of high, moderate, low burn severity, and unburned areas and the Landsat-based MTBS burn severity product tends to show comprehensive burned effects at the plot scale (i.e. 30 m) by incorporating multiple strata (Cocke et al., 2005; Lentile et al., 2009), leading to a substantial

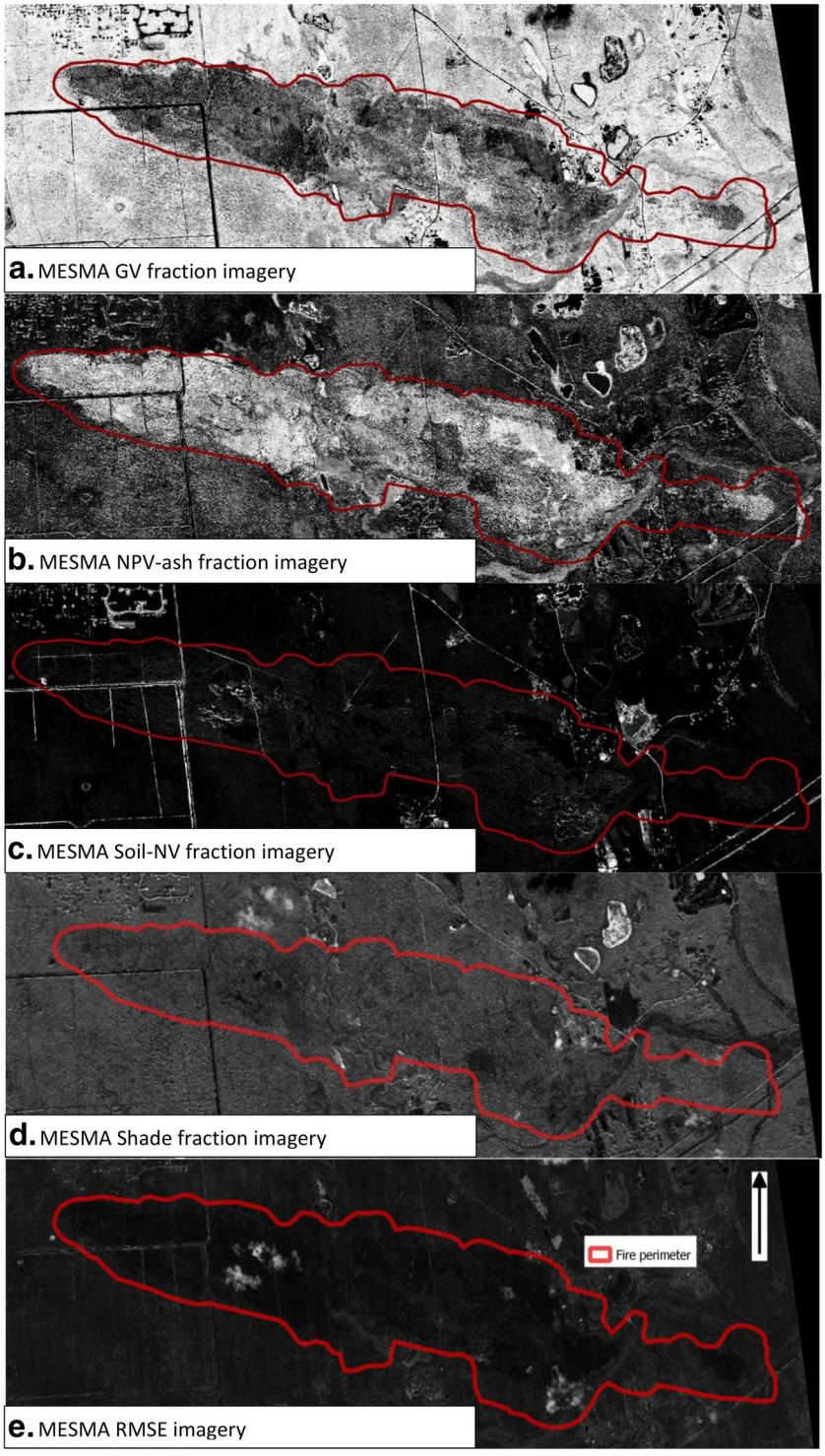

Fig. 7. MESMA fraction images from the post-fire WV-2 imagery in 2012.

underestimation of high severity area at the crown scale and the overestimation of the area burned at moderate severity in this study (Fig. 8). Although with many similarities, the burn severity definition used for our WV-2-based burn severity map was also not the same as the MTBS burn severity product (Eidenshink et al., 2007). These together make the general spatial pattern in burned effects between our WV-2-based and the Landsat-based burn severity map comparable (Fig. 8), but many differences in spatial details. Similarly, during our field data survey of the burn, we found that heterogeneous regrowth patterns were apparent within our 15 m by 15 m fixed-area plots, consistent with heterogeneous patterns of damaged or survived trees (Cocke et al., 2005). We also observed that some trees had become standing-dead (i.e. snag) with no sign of recovery (e.g. no resprout or leaf out) while some oaks resprouted vigorously from the root crown after being top-killed. In addition, some trees that experienced crown scorching, particularly pitch pine, were able to sprout from basal and epicormic buds on the bole and remaining branches. In the future, we will explore these detailed recovery patterns in more detail for this study area using multi-sensor G-LiHT imagery. We will use this data to explore what varying

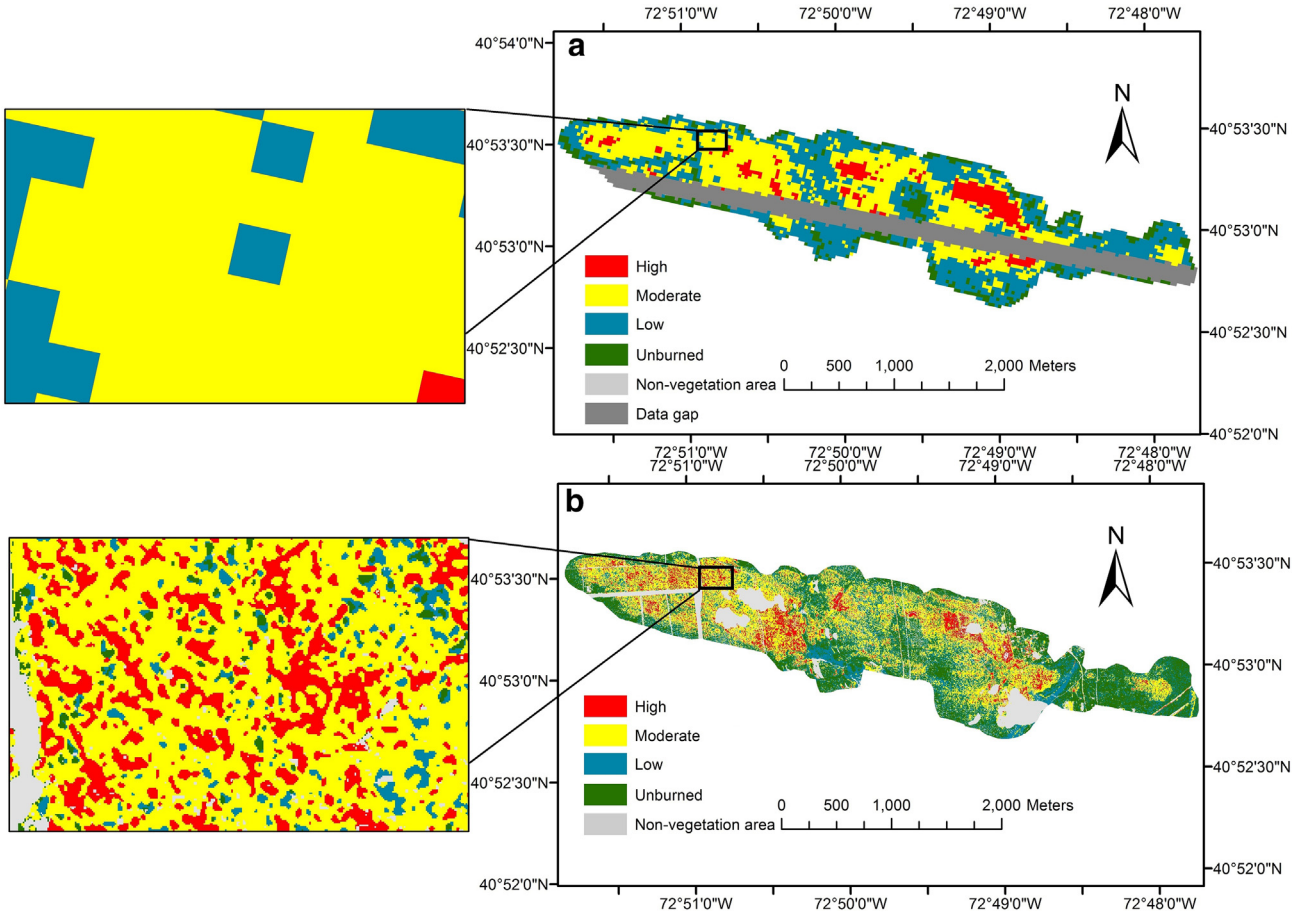

Fig. 8. Burn severity maps. a. Landsat dNBR from MTBS; b. WV-2 ΔMSAVI and MESMA. Non-vegetation pixels (e.g. road, buildup areas, shadow, cloud) were masked from the WV-2 burn severity map (see Section 3.2.1). The data gap on Landsat burn severity map is due to the scan line corrector failure of enhanced thematic mapper plus of Landsat-7 on the post-fire imagery in 2012.

burned effects actually mean for post-fire recovery, in terms of forest structure, function, and composition.

Consistent with the recent suggestions by Morgan et al. (2014) towards more ecologically based severity classifications, we directly established three levels of burn severity, showing actual ecological effects (e.g. tree mortality, non-foliated/brown canopy) on the post-fire 0.10 m aerial ortho-photos at a relevant spatial scale to trees been damaged. Both MESMA fractions and the targeted ΔSI (i.e. MSAVI) were found to be useful for mapping burn severity in this study. During the RF OOB error estimation, MESMA fractions showed lower OOB error (higher accuracy), compared to ΔSI, because they were analogous to the definition of burn severity used in this study and made use of the full post-fire spectra (Lentile et al., 2006; Quintano et al., 2013), rather than two or three spectral bands; on the other hand, the combination of ΔSI and MESMA fractions showed the lowest OOB error (highest accuracy), as ΔSI provided additional information on the canopy loss by fire (Lentile et al., 2006; White et al., 1996). However, the performances of MESMA fractions and Δ SI for mapping burn severity from VHR data still required more studies in other fire-prone ecosystems or fire regimes, like Mediterranean chaparral and Boreal black spruce ecosystems, considering the differences in fire behaviors and plant traits.

Table 7
Producer Accuracy (PA) (percent) and User Accuracy (UA) (percent) per class of burn severity level, Overall Accuracy (OA), and Kappa coefficient of burn severity level estimates at the sub-crown and crown scales.

	Sub-crown				Crown			
	U	L	M	H	U	L	M	H
PA	84	77	79	97	90	75	75	89
UA	89	77	85	84	93	50	70	89
OA	84				82			
Kappa	0.77				0.76			

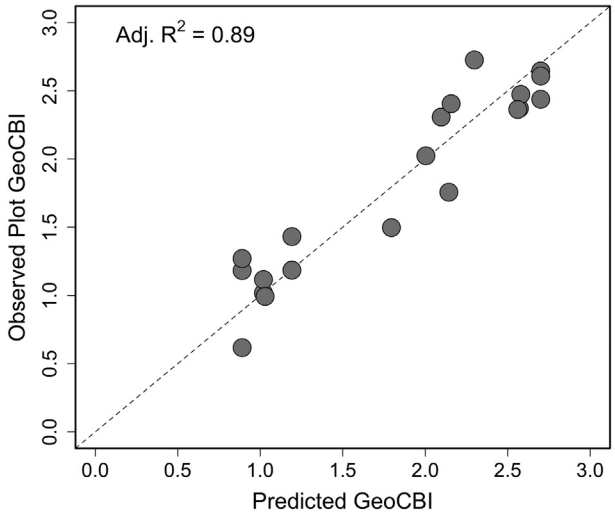

Fig. 9. Scatterplot of plot GeoCBI ratings estimated from the black/brown tree percentage within field plot and corresponding OLS model predicted values. The adjusted R-squared of the OLS model for predicting plot GeoCBI ratings is also included. (For interpretation of the references to color in this figure legend, the reader is referred to the web version of this article.)

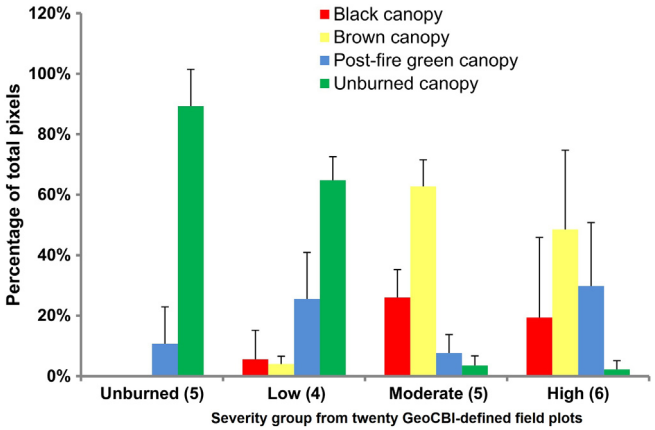

Fig. 10. Mean percentages of canopy class pixels (black canopy (H), brown canopy (M), post-fire green canopy (L), and unburned canopy (U)) in each severity group from twenty GeoCBI-defined field plots. Error bars indicate standard deviations. Numbers along with the severity group indicate the number of field plots included in corresponding group. (For interpretation of the references to color in this figure legend, the reader is referred to the web version of this article.)

In our study, we also assessed the separability of multiple SIs in discriminating burned effects at fine spatial scales in our coastal Pine Barrens ecosystem. We found that SIs (e.g. MSAVI, SAVI), designed to account for the proportion of background reflectance from under-canopy (e.g. soil, vegetation, and shadow), tended to show higher separability (Table 4). These SIs with high discrimination power also depended on the differences between NIR and red reflectance values: a noticeable decrease in NIR and red spectral reflectance have been detected previously as a result of fire using a range of imagery (Lentile et al., 2006; Serbin et al., 2013; White et al., 1996). This conclusion is consistent with Schepers et al. (2014) and Arnett et al. (2015)'s finding using VHR imagery for assessing burned effects in heathlands of Europe and a mixed forest of western Canada, respectively. Compared with other forest disturbances (e.g. insect herbivory), fire can be a stand-replacing disturbance drastically affecting the physical, biophysical and spectral properties of the land surface in the short to long term (e.g. Amiro et al., 2006; Goulden et al., 2006). Within a reasonably closed forest (LAI > 2), tree crowns dominate surface reflectance, however following fire or other disturbances, background effects from under-canopy, such as increased areal cover of burnt duff, soil exposure, charred residue, and soil color alteration, can add substantial variations in spectral reflectance to remotely sensed imagery, especially at fine spatial scales (Holden et al., 2010). As a result, SIs (e.g. SAVI and MSAVI), designed to account for the proportion of background reflectance from under-canopy, demonstrated better performances in the discrimination of burned effects than the other traditional SIs (e.g. NDVI) from VHR imagery (Arnett et al., 2015; Schepers et al., 2014; this study). Some other SIs were not originally designed to be used for our study area (e.g. BAI) or for post-fire studies from VHR sensors (e.g. EVI), and the default convergence values (L) for SIs calculations were also used without recalibration. But similar to this study, Holden et al. (2010) and Arnett et al. (2015) adapted EVI for detecting burned effects with relatively high accuracy using VHR sensors. Fine-tuning of SI calculations could result in improved performance for discriminating burned effects, but this may come at a cost of adaptability to other sites and a careful exploration of the need for tuning is needed but beyond this scope of this study.

Previous studies demonstrated that the performance of SIs for burn severity assessment depended on vegetation type at both a moderate resolution (Epting et al., 2005; Hammill and Bradstock, 2006) and VHR level (Schepers et al., 2014). But our results showed that tree species had little effect on the SI separation power, and thus SI from VHR data can be potentially used as a general method for discriminating burned areas in mixed forest ecosystems; but these needs further exploration in more diverse forest ecosystems. The lower M values when taking species into account (Table 4 and Table 5) come from the fact that the error of visual inspection on tree species can bring more extreme values for species level M calculations (relatively increased standard deviations).

6. Conclusion

Our study significantly contributes to the continued efforts for assessing the ecological, management, and policy implications of forest disturbances and extends our understanding of forest burn severity assessment at fine spatial scales. Compared with previous studies using VHR or hyperspectral imagery for assessing burn severity, e.g., (Chen et al., 2015b; Holden et al., 2010; Schepers et al., 2014), for the first time, we establish a pixel-based approach to map forest burn severity at fine spatial scales, using the combination of bi-temporal VHR imagery (i.e. WV-2), post-fire aerial ortho-photos, and ground survey data. Our results showed that 1) ΔSI, designed to minimize the effects of background reflectance (e.g. MSAVI and SAVI) can be effectively used for discriminating burned effects at the sub-crown scale in a Pine Barrens ecosystem, consistent with similar studies in other ecosystem types (Arnett et al., 2015; Schepers et al., 2014). Furthermore, tree species had little effect on its discrimination power; 2) MESMA fractions from VHR data (i.e. WV-2) had a high predictive power for mapping forest burn severity with the targeted ΔSI (i.e. ΔMSAVI); 3) our pixel-wise approach from VHR data (i.e. WV-2) can be used for mapping forest burn severity at fine spatial scales and the mapping result is consistent across spatial scales (i.e. from sub-crown to crown to inter-crown). Future work should explore the use of VHR imagery with short-wave-infrared bands (e.g. WorldView-3) which could produce even more accurate post-fire mapping using SI-based method, however a modified version of NBR accounting for heterogeneous spectral features of burned areas may be needed. Additional studies are needed to further explore ecologically meaningful ground measurements of burn severity (e.g. tree mortality percentage, live basal area, diameter of the smallest remaining branches) for remote sensing of burn severity at fine spatial scales (Morgan et al., 2014); the linkage and sensitivity of different remotely sensed measurements can thus be extensively explored across various spatial scales and ecosystems.

Acknowledgement

We thank the following data providers. DigitalGlobe data were provided by NASA's NGA Commercial Archive Data (cad4nasa.gsfc.nasa.gov) under the National Geospatial Intelligence Agency's NextView license agreement. Post-fire aerial color ortho-photos were provided by New York Statewide Digital Ortho-imagery Program. Financial support for this research was provided by the U.S. Department of Energy contract No. DE-SC00112704 to Brookhaven National Laboratory

References

Amiro, B.D., Orchansky, A.L., Barr, A.G., Black, T.A., Chambers, S.D., Chapin III, F.S., Gouldenf, M.L., Litvakg, M., Liu, H.P., McCaughey, J.H., McMillan, A., Randerson, J.T., 2006. The effect of post-fire stand age on the boreal forest energy balance. Agric. For. Meteorol. 140, 41–50.

Arnett, J., Coops, N.C., Daniels, L.D., Falls, R.W., 2015. Detecting forest damage after a low-severity fire using remote sensing at multiple scales. Int. J. Appl. Earth Obs. Geoinf. 35, 239–246.

Bowman, D.M.J.S., Balch, J.K., Artaxo, P., Bond, W.J., Carlson, J.M., Cochrane, M.A., D'Antonio, C.M., DeFries, R.S., Doyle, J.C., Harrison, S.P., Johnston, F.H., Keeley, J.E., Krawchuk, M.A., Kull, C.A., Marston, J.B., Moritz, M.A., Prentice, I.C., Roos, C.I., Scott, A.C., Swetnam, T.W., Van Der Werf, G.R., Pyne, S.J., 2009. Fire in the earth system. Science 324, 481–484.

Breiman, L., 2001. Random forests. Mach. Learn. 45, 5–32.

Brewer, C.K., Winne, J.C., Redmond, R.L., Opitz, D.W., Mangrich, M.V., 2005. Classifying and mapping wildfire severity: a comparison of methods. Photogramm. Eng. Remote. Sens. 71, 1311–1320.

Canty, M.J., Nielsen, A.A., 2008. Automatic radiometric normalization of multitemporal satellite imagery with the iteratively re-weighted MAD transformation. Remote Sens. Environ. 112, 1025–1036.
Chen, G., Metz, M.R., Rizzo, D.M., Dillon, W.W., Meentemeyer, R.K., 2015a. Object-based assessment of burn severity in diseased forests using high-spatial and high-spectral resolution MASTER airborne imagery. ISPRS J. Photogramm. Remote Sens. 102, 38–47.
Chen, G., Metz, M.R., Rizzo, D.M., Meentemeyer, R.K., 2015b. Mapping burn severity in a disease-impacted forest landscape using Landsat and MASTER imagery. Int. J. Appl. Earth Obs. Geoinf. 40, 91–99.
Cho, M.A., Malahlela, O., Ramoelo, A., 2015. Assessing the utility WorldView-2 imagery for tree species mapping in South African subtropical humid forest and the conservation implications: Dukuduku forest patch as case study. Int. J. Appl. Earth Obs. Geoinf. 38, 349–357.
Chuvieco, E., Martin, M.P., Palacios, A., 2002. Assessment of different spectral indices in the red-near-infrared spectral domain for burned land discrimination. Int. J. Remote Sens. 23, 5103–5110.
Chuvieco, E., Riaño, D., Danson, F., Martin, P., 2006. Use of a radiative transfer model to simulate the postfire spectral response to burn severity. J. Geophys. Res. Biogeosci. 111.
Cocke, A.E., Fule, P.Z., Crouse, J.E., 2005. Comparison of burn severity assessments using differenced normalized burn ratio and ground data. Int. J. Wildland Fire 14, 189–198.
Congalton, R.G., 1991a. Remote sensing and geographic information system data integration: Error sources and research issues. Photogramm. Eng. Remote Sens. 57, 677–687.
Congalton, R.G., 1991b. A review of assessing the accuracy of classifications of remotely sensed data. Remote Sens. Environ. 37, 35–46.
Cook, B.D., Nelson, R.F., Middleton, E.M., Morton, D.C., McCorkel, J.T., Masek, J.G., Ranson, K.J., Ly, V., Montesano, P.M., 2013. NASA Goddard's lidar, hyperspectral and thermal (G-LiHT) airborne imager. Remote Sens. 5, 4045–4066.
Coops, N.C., Johnson, M., Wulder, M.A., White, J.C., 2006. Assessment of QuickBird high spatial resolution imagery to detect red attack damage due to mountain pine beetle infestation. Remote Sens. Environ. 103, 67–80.
Craney, T.A., Surles, J.G., 2002. Model-dependent variance inflation factor cutoff values. Qual. Eng. 14, 391–403.
Davranche, A., Lefebvre, G., Poulin, B., 2010. Wetland monitoring using classification trees and SPOT-5 seasonal time series. Remote Sens. Environ. 114, 552–562.
De Santis, A., Chuvieco, E., 2009a. GeoCBI: a modified version of the Composite Burn Index for the initial assessment of the short-term burn severity from remotely sensed data. Remote Sens. Environ. 113, 554–562.
De Santis, A., Chuvieco, E., Vaughan, P.J., 2009b. Short-term assessment of burn severity using the inversion of PROSPECT and GeoSail models. Remote Sens. Environ. 113, 126–136.
Dennison, P.E., Roberts, D.A., 2003. Endmember selection for multiple endmember spectral mixture analysis using endmember average RMSE. Remote Sens. Environ. 87, 123–135.
Dennison, P.E., Halligan, K.Q., Roberts, D.A., 2004. A comparison of error metrics and constraints for multiple endmember spectral mixture analysis and spectral angle mapper. Remote Sens. Environ. 93, 359–367.
Dragozi, E., Gitas, I.Z., Bajocco, S., Stavrakoudis, D.G., 2016. Exploring the relationship between burn severity field data and very high resolution GeoEye images: the case of the 2011 Evros Wildfire in Greece. Remote Sens. 8 (7), 566.
Drake, N.A., Mackin, S., Settle, J.J., 1999. Mapping vegetation, soils, and geology in semiarid shrublands using spectral matching and mixture modeling of SWIR AVIRIS imagery. Remote Sens. Environ. 68, 12–25.
Dudley, K.L., Dennison, P.E., Roth, K.L., Roberts, D.A., Coates, A.R., 2015. A multi-temporal spectral library approach for mapping vegetation species across spatial and temporal phenological gradients. Remote Sens. Environ. 167, 121–134.
Eidenshink, J., Schwind, B., Brewer, K., Zhu, Z., Quayle, B., Howard, S., 2007. A project for monitoring trends in burn severity. Fire Ecol. 3, 3–21.
Epting, J., Verbyla, D., Sorbel, B., 2005. Evaluation of remotely sensed indices for assessing burn severity in interior Alaska using Landsat TM and ETM+. Remote Sens. Environ. 96, 328–339.
Fernandez-Manso, A., Quintano, C., Roberts, D.A., 2016. Burn severity influence on post-fire vegetation cover resilience from Landsat MESMA fraction images time series in Mediterranean forest ecosystems. Remote Sens. Environ. 184, 112–123.
Flannigan, M.D., Stocks, B.J., Wotton, B.M., 2000. Climate change and forest fires. Sci. Total Environ. 262, 221–229.
Frolking, S., Palace, M.W., Clark, D.B., Chambers, J.Q., Shugart, H.H., Hurtt, G.C., 2009. Forest disturbance and recovery: a general review in the context of spaceborne remote sensing of impacts on aboveground biomass and canopy structure. J. Geophys. Res. G: Biogeosci. 114.
Goulden, M.L., Winston, G.C., McMillan, A.M.S., Litvak, M.E., Read, E.L., Rocha, A.V., Elliot, J.R., 2006. An eddy covariance mesonet to measure the effect of forest age on land-atmosphere exchange. Glob. Chang. Biol. 12, 2146–2162.
Griffith, D.A., Peres-Neto, P.R., 2006. Spatial modeling in ecology: The flexibility of eigenfunction spatial analyses. Ecology 87 (10), 2603–2613.
Hammill, K.A., Bradstock, R.A., 2006. Remote sensing of fire severity in the Blue Mountains: influence of vegetation type and inferring fire intensity. Int. J. Wildland Fire 15, 213–226.
Hart, S.J., Veblen, T.T., 2015. Detection of spruce beetle-induced tree mortality using high- and medium-resolution remotely sensed imagery. Remote Sens. Environ. 168, 134–145.
Holden, Z.A., Morgan, P., Smith, A.M., Vierling, L., 2010. Beyond Landsat: a comparison of four satellite sensors for detecting burn severity in ponderosa pine forests of the Gila Wilderness, NM, USA. Int. J. Wildland Fire 19, 449–458.
Huete, A.R., 1988. A soil-adjusted vegetation index (SAVI). Remote Sens. Environ. 25, 295–309.
Huete, A., Didan, K., Miura, T., Rodriguez, E.P., Gao, X., Ferreira, L.G., 2002. Overview of the radiometric and biophysical performance of the MODIS vegetation indices. Remote Sens. Environ. 83, 195–213.
Jin, S.M., Sader, S.A., 2005. Comparison of time series tasseled cap wetness and the normalized difference moisture index in detecting forest disturbances. Remote Sens. Environ. 94, 364–372.
Jordan, M.J., Patterson, W.A., Windisch, A.G., 2003. Conceptual ecological models for the Long Island pitch pine barrens: Implications for managing rare plant communities. For. Ecol. Manag. 185, 151–168.
Keeley, J.E., 2009. Fire intensity, fire severity and burn severity: A brief review and suggested usage. Int. J. Wildland Fire 18, 116–126.
Key, C.H., Benson, N.C., 2006. Landscape assessment:sampling and analysis methods. Rocky Mountain Research Station General Technical Report, RMRS-GTR-164-CD.
Klonus, S., Ehlers, M., 2009. Performance of evaluation methods in image fusion. Information Fusion, 2009. FUSION'09. 12th International Conference on (pp. 1409–1416): IEEE.
Kurczewski, F.E., Boyle, H.F., 2000. Historical changes in the pine barrens of central Suffolk County, New York. Northeast. Nat. 7, 95–112.
Lawrence, R.L., Wood, S.D., Sheley, R.L., 2006. Mapping invasive plants using hyperspectral imagery and Breiman Cutler classifications (RandomForest). Remote Sens. Environ. 100, 356–362.
Lentile, L.B., Holden, Z.A., Smith, A.M.S., Falkowski, M.J., Hudak, A.T., Morgan, P., Lewis, S.A., Gessler, P.E., Benson, N.C., 2006. Remote sensing techniques to assess active fire characteristics and post-fire effects. Int. J. Wildland Fire 15, 319–345.
Lentile, L.B., Smith, A.M., Hudak, A.T., Morgan, P., Bobbitt, M.J., Lewis, S.A., Robichaud, P.R., 2009. Remote sensing for prediction of 1-year post-fire ecosystem condition. Int. J. Wildland Fire 18 (5), 594–608.
Lu, B., He, Y., Tong, A., 2015. Evaluation of spectral indices for estimating burn severity in semiarid grasslands. Int. J. Wildland Fire 25, 147–157.
Marvin, D.C., Asner, G.P., Schnitzer, S.A., 2016. Liana canopy cover mapped throughout a tropical forest with high-fidelity imaging spectroscopy. Remote Sens. Environ. 176, 98–106.
Meng, R., Dennison, P.E., 2015. Spectroscopic analysis of green, desiccated and dead tamarisk canopies. Photogramm. Eng. Remote Sens. 81, 199–207.
Meng, R., Dennison, P., Jamison, L., van Riper, C., Nager, P., Hultine, K., Bean, D., Dudley, T., 2012. Detection of tamarisk defoliation by the northern tamarisk beetle based on multitemporal Landsat 5 thematic mapper imagery. GIScience Remote Sens. 49, 510–537.
Meng, R., Dennison, P.E., Huang, C., Moritz, M.A., D'Antonio, C., 2015. Effects of fire severity and post-fire climate on short-term vegetation recovery of mixed-conifer and red fir forests in the Sierra Nevada Mountains of California. Remote Sens. Environ. 171, 311–325.
Miller, J.D., Thode, A.E., 2007. Quantifying burn severity in a heterogeneous landscape with a relative version of the delta Normalized Burn Ratio (dNBR). Remote Sens. Environ. 109, 66–80.
Miller, J.D., Knapp, E.E., Key, C.H., Skinner, C.N., Isbell, C.J., Creasy, R.M., Sherlock, J.W., 2009. Calibration and validation of the relative differenced Normalized Burn Ratio (RdNBR) to three measures of fire severity in the Sierra Nevada and Klamath Mountains, California, USA. Remote Sens. Environ. 113, 645–656.
Mitri, G.H., Gitas, I.Z., 2006. Fire type mapping using object-based classification of Ikonos imagery. Int. J. Wildland Fire 15, 457–462.
Mitri, G.H., Gitas, I.Z., 2008. Mapping the severity of fire using object-based classification of IKONOS imagery. Int. J. Wildland Fire 17, 431–442.
Mitri, G.H., Gitas, I.Z., 2013. Mapping post-fire forest regeneration and vegetation recovery using a combination of very high spatial resolution and hyperspectral satellite imagery. Int. J. Appl. Earth Obs. Geoinf. 20, 60–66.
Morgan, P., Keane, R.E., Dillon, G.K., Jain, T.B., Hudak, A.T., Karau, E.C., Sikkink, P.G., Holden, Z.A., Strand, E.K., 2014. Challenges of assessing fire and burn severity using field measures, remote sensing and modelling. Int. J. Wildland Fire 23, 1045–1060.
Norton, J., Glenn, N., Germino, M., Weber, K., Seefeldt, S., 2009. Relative suitability of indices derived from Landsat ETM+ and SPOT 5 for detecting fire severity in sagebrush steppe. Int. J. Appl. Earth Obs. Geoinf. 11, 360–367.
Pal, M., 2005. Random forest classifier for remote sensing classification. Int. J. Remote Sens. 26, 217–222.
Pereira, J.M.C., 1999. A comparative evaluation of NOAA/AVHRR vegetation indexes for burned surface detection and mapping. IEEE Trans. Geosci. Remote Sens. 37, 217–226.
Pérez-Cabello, F., Cerdà, A., De la Riva, J., Echeverría, M., García-Martín, A., Ibarra, P., Lasanta, T., Montorio, R., Palacios, V., 2012. Micro-scale post-fire surface cover changes monitored using high spatial resolution photography in a semiarid environment: a useful tool in the study of post-fire soil erosion processes. J. Arid Environ. 76, 88–96.
Qi, J., Chehbouni, A., Huete, A., Kerr, Y., Sorooshian, S., 1994. A modified soil adjusted vegetation index. Remote Sens. Environ. 48, 119–126.
Quintano, C., Fernández-Manso, A., Roberts, D.A., 2013. Multiple Endmember Spectral Mixture Analysis (MESMA) to map burn severity levels from Landsat images in Mediterranean countries. Remote Sens. Environ. 136, 76–88.
Reiners, W., 1967. Relationships between vegetational strata in the pine barrens of central Long Island, New York. Bull. Torrey. Bot. Club 87–99.
Riaño, D., Chuvieco, E., Ustin, S., Zomer, R., Dennison, P., Roberts, D., Salas, J., 2002. Assessment of vegetation regeneration after fire through multitemporal analysis of AVIRIS images in the Santa Monica Mountains. Remote Sens. Environ. 79, 60–71.
Roberts, D.A., Gardner, M., Church, R., Ustin, S., Scheer, G., Green, R.O., 1998. Mapping Chaparral in the Santa Monica Mountains using multiple endmember spectral mixture models. Remote Sens. Environ. 65, 267–279.

Roberts, D.A., Dennison, P.E., Gardner, M.E., Hetzel, Y., Ustin, S.L., Lee, C.T., 2003. Evaluation of the potential of Hyperion for fire danger assessment by comparison to the airborne visible/infrared imaging spectrometer. IEEE Trans. Geosci. Remote Sens. 41, 1297–1310.

Roberts, D.A., Halligan, K., Dennison, P.E., 2007. VIPER Tools User Manual (Version1. 5).

Roberts, D.A., Dennison, P.E., Roth, K.L., Dudley, K., Hulley, G., 2015. Relationships between dominant plant species, fractional cover and land surface temperature in a Mediterranean ecosystem. Remote Sens. Environ. 167, 152–167.

Schepers, L., Haest, B., Veraverbeke, S., Spanhove, T., Vanden Borre, J., Goossens, R., 2014. Burned area detection and burn severity assessment of a heathland fire in Belgium using airborne imaging spectroscopy (APEX). Remote Sens. 6, 1803–1826.

Schroeder, T.A., Cohen, W.B., Song, C., Canty, M.J., Yang, Z., 2006. Radiometric correction of multi-temporal Landsat data for characterization of early successional forest patterns in western Oregon. Remote Sens. Environ. 103, 16–26.

Serbin, S.P., Ahl, D.E., Gower, S.T., 2013. Spatial and temporal validation of the MODIS LAI and FPAR products across a boreal forest wildfire chronosequence. Remote Sens. Environ. 133, 71–84.

Settle, J., Campbell, N., 1998. On the errors of two estimators of sub-pixel fractional cover when mixing is linear. IEEE Trans. Geosci. Remote Sens. 36, 163–170.

Smith, A.M.S., Lentile, L.B., Hudak, A.T., Morgan, P., 2007. Evaluation of linear spectral unmixing and DNBR for predicting postfire recovery in a North American ponderosa pine forest. Int. J. Remote Sens. 28, 5159–5166.

Smith, A.M., Sparks, A.M., Kolden, C.A., Abatzoglou, J.T., Talhelm, A.F., Johnson, D.M., Boschetti, L., Lutz, J.A., Apostol, K.G., Yedinak, K.M., 2016. Towards a new paradigm in fire severity research using dose–response experiments. Int. J. Wildland Fire.

Sparks, A.M., Kolden, C.A., Talhelm, A.F., Smith, A., Apostol, K.G., Johnson, D.M., Boschetti, L., 2016. Spectral indices accurately quantify changes in seedling physiology following fire: towards mechanistic assessments of post-fire carbon cycling. Remote Sens. 8, 572.

Speybroeck, N., 2012. Classification and regression trees. Int. J. Public Health 57, 243–246.

Sugihara, N.G., Wagtendonk, J.W.V., Fites-Kaufman, J., 2006. Fire as ecological process. In: Sugihara, N.G., Wagtendonk, J.W.V., Shaffer, K.E., Fites-Kaufman, J., Andrea, E.T. (Eds.), Fire in California's Ecosystems. University of California Press, Berkeley Los Angeles London.

Team, R.C., 2013. R: A Language and Environment for Statistical Computing.

Tucker, C.J., 1979. Red and photographic infrared linear combinations for monitoring vegetation. Remote Sens. Environ. 8, 127–150.

Van Wagtendonk, J.W., Root, R.R., Key, C.H., 2004. Comparison of AVIRIS and Landsat ETM+ detection capabilities for burn severity. Remote Sens. Environ. 92, 397–408.

Veraverbeke, S., Hook, S., Hulley, G., 2012. An alternative spectral index for rapid fire severity assessments. Remote Sens. Environ. 123, 72–80.

Werf, V.D., Randerson, G.R., Giglio, J.T., Collatz, L., Mu, G.J., Kasibhatla, M., Morton, D.C., DeFries, R.S., van Jin, Y., van Leeuwen, T.T., 2010. Global fire emissions and the contribution of deforestation, savanna, forest, agricultural, and peat fires (1997–2009). Atmos. Chem. Phys. 10, 11707–11735.

White, J.D., Ryan, K.C., Key, C.C., Running, S.W., 1996. Remote sensing of forest fire severity and vegetation recovery. Int. J. Wildland Fire 6, 125–136.

Whitman, E., Rapaport, E., Sherren, K., 2013. Modeling fire susceptibility to delineate Wildland-urban Interface for municipal-scale fire risk management. Environ. Manag. 52, 1427–1439.

Whittaker, R.H., Woodwell, G.M., 1969. Structure, production and diversity of the oak-pine Forest at Brookhaven, New York. J. Ecol. 57, 155–174.

Wilson, A.M., Latimer, A.M., Silander, J.A., 2015. Climatic Controls on Ecosystem Resilience: Postfire Regeneration in the Cape Floristic Region of South Africa. Proceedings of the National Academy of Sciences of the United States of America 112 pp. 9058–9063.

Wulder, M.A., White, J.C., Coops, N.C., Butson, C.R., 2008. Multi-temporal analysis of high spatial resolution imagery for disturbance monitoring. Remote Sens. Environ. 112, 2729–2740.

Yu, X., Hyyppä, J., Vastaranta, M., Holopainen, M., Viitala, R., 2011. Predicting individual tree attributes from airborne laser point clouds based on the random forests technique. ISPRS J. Photogramm. Remote Sens. 66, 28–37.